



Article

Detection of Winter Heat Wave Impact on Surface Runoff in a Periglacial Environment (Ny-Ålesund, Svalbard)

Roberto Salzano ^{1,*}, Riccardo Cerrato ^{1,2}, Federico Scoto ^{3,4}, Andrea Spolaor ^{4,5}, Emiliana Valentini ⁵, Marco Salvatore ⁶, Giulio Esposito ¹, Serena Sapio ⁶, Andrea Taramelli ^{5,6} and Rosamaria Salvatori ⁵

¹ Institute of Atmospheric Pollution Research, National Research Council of Italy, Sesto Fiorentino, 50019 Florence, Italy; riccardo.cerrato@unipi.it (R.C.); esposito@iia.cnr.it (G.E.)

² Department of Earth Sciences, University of Pisa, 56126 Pisa, Italy

³ Institute of Atmospheric and Climate Sciences, National Research Council of Italy, 73100 Lecce, Italy; federico.scoto@unive.it

⁴ Department of Environmental Sciences, Informatics and Statistics, Ca' Foscari University of Venice, 30173 Venice, Italy; andrea.spolaor@cnr.it

⁵ Institute of Polar Science, National Research Council of Italy, 30172 Venice, Italy; emiliana.valentini@cnr.it (E.V.); andrea.taramelli@iusspavia.it (A.T.); rosamaria.salvatori@cnr.it (R.S.)

⁶ Institute for Advanced Study of Pavia—IUSS, 27100 Pavia, Italy; marco.salvadore@uniroma1.it (M.S.); serena.sapio@iusspavia.it (S.S.)

* Correspondence: roberto.salzano@cnr.it; Tel.: +39-055226587

Abstract: The occurrence of extreme warm events in the Arctic has been increasing in recent years in terms of their frequency and intensity. The assessment of the impact of these episodes on the snow season requires further observation capabilities, where spatial and temporal resolutions are key constraints. This study targeted the snow season of 2022 when a winter rain-on-snow event occurred at Ny-Ålesund in mid-March. The selected methodology was based on a multi-scale and multi-platform approach, combining ground-based observations with satellite remote sensing. The ground-based observation portfolio included meteorological measurements, nivological information, and the optical description of the surface in terms of spectral reflectance and snow-cover extent. The satellite data were obtained by the Sentinel-2 platforms, which provided ten multi-spectral acquisitions from March to July. The proposed strategy supported the impact assessment of heat waves in a periglacial environment, describing the relation and the timing between rain-on-snow events and the surface water drainage system. The integration between a wide range of spectral, time, and spatial resolutions enhanced the capacity to monitor the evolution of the surface water drainage system, detecting two water discharge pulsations, different in terms of duration and effects. This preliminary study aims to improve the description of the snow dynamics during those extreme events and to assess the impact of the produced break during the snow accumulation period.

Keywords: snow cover; rain on snow; snow melting; surface water runoff



Citation: Salzano, R.; Cerrato, R.; Scoto, F.; Spolaor, A.; Valentini, E.; Salvatore, M.; Esposito, G.; Sapio, S.; Taramelli, A.; Salvatori, R. Detection of Winter Heat Wave Impact on Surface Runoff in a Periglacial Environment (Ny-Ålesund, Svalbard). *Remote Sens.* **2023**, *15*, 4435. <https://doi.org/10.3390/rs15184435>

Academic Editor: Ulrich Kamp

Received: 30 June 2023

Revised: 25 August 2023

Accepted: 7 September 2023

Published: 9 September 2023



Copyright: © 2023 by the authors. Licensee MDPI, Basel, Switzerland. This article is an open access article distributed under the terms and conditions of the Creative Commons Attribution (CC BY) license (<https://creativecommons.org/licenses/by/4.0/>).

1. Introduction

During the past decades, the Arctic region has been undergoing a significant transformation [1,2] associated with the onset of a climatic phenomenon defined as Arctic Amplification [3]. The overall increase in regional temperatures is a framework that includes extreme events, characterized by persistent warm and moist air masses occurring during the summer and, recently, also during the winter season. The broader term used for these anomalous periods is ‘warm spell’, even if the most extreme events are sometimes differentiated as heat waves (HWs) [4]. These terms share the definition based on prolonged periods of unusually elevated temperatures, where a large variety of metrics are focused on the assessment of their severity [5]. HWs are often associated with rainfall

events, and they pose a multitude of environmental, ecological, and socio-economic challenges to the fragile Arctic ecosystem and its inhabitants [6–8]. These events were largely observed in some of the most sensitive regions in terms of climate system [9], i.e., in the northern maritime regions (such as Scandinavia, Canada, Greenland, and Spitsbergen) [1,2]. While the occurrence and frequency of winter heat waves are unpredictable, the impact is widely distributed across coastal and inland mountain regions [10]. Several studies have documented the negative effects of HWs associated with rainfall on small and large herbivores, soil invertebrates, vegetation growth, and reproduction [11,12]. The snow cover loss during a midwinter heat wave can, in fact, trigger physiological activity in organisms that should be generally dormant; this is the case of lichens, generally considered highly resistant to frost and drought, which are physiologically activated, even during the dark polar winters [13], in the case of increased heat and water transfer to the snow–ground interface. In contrast, some other ecological components like mosses, typically growing in habitats with deep snow cover, are more exposed to cold spells when a thinner and less insulating snowpack occurs [11]. The primary impact of HWs on the snow cover is the development of basal ice layers, which can also have serious socio-economic feedback for reindeer herders but also for the tourism industry and local communities in the Arctic [14].

Extreme events are related to meteo-climatic conditions [3–5] driving a transfer of northerly air masses which are warmer and wetter than usual [15]. These phenomena have been increasing in the last decade, also due to a simultaneous reduction in sea ice [16]. Oceans lacking sea ice are warming more rapidly, thus facilitating water evaporation as well as the alteration of the atmospheric circulation, contributing to the occurrence of HWs with both higher frequency and intensity [16,17]. The association with rain-on-snow (RoS) episodes [18] impacts the cryosphere, both on terrestrial ecosystems in snow-free areas and during the summer season and in snow-covered areas. Generally, when rain falls on an existing snow cover, it produces hard crusts on the snow surface or water percolation through the snowpack, with pools at the snow–ground interface [18]. The ultimate impact of these events involves the alteration of the snow–albedo feedback and the acceleration of the hydrological cycle associated with the snow melting [19]. Winter heat waves and, eventually, RoS events affect the snow season, producing discontinuities in the snow accumulation phase, affecting moistening and ripening processes on the first level, and then triggering a water runoff through the snowpack. The presence of water in the snowpack implies state transformations and a heat transfer process even at the level of the snow–ground interface, producing soil warming and permafrost thawing [20]. Monitoring the snow dynamics during the whole accumulation and melting periods with particular attention to the winter season and to the occurrence of HWs and RoS constitutes primary knowledge in understanding HW characteristics, also in terms of changes in their frequency and severity, as well as their different impacts [21]. Nowadays, the investigation of RoS events is based on meteorological station records, on local and indigenous knowledge holders, on satellite remote sensing, and on atmospheric reanalysis.

While the identification of RoS events is a well-developed issue [22], their impact assessment on the surface requires further efforts. A snow-cover extent (SCE) evaluation is the primary element to estimate the size of a surface covered by snow in a defined area of interest: this is an Essential Climate Variable (ECV), as listed by the Global Climate Observing System (GCOS) [23], and its estimation is generally approached using binary snow products or fractional cover maps [24,25]. Temporal and spatial resolutions are the key aspects that affect the selection of the most appropriate methodology. Optical sensors are largely used for this purpose, but resolutions are biased by observing geometries, illumination conditions (sun elevation and cloud cover) [26], and surface properties (slope orientation and inclination). Satellite, airborne, or ground-based platforms support different resolutions, varying from coarse (above 250 m), medium (from 10 m to 250 m), to high (below 10 m) spatial pixel sizes. The temporal resolution ranges from low (more than 5 days) to high (daily), depending on the platform specifics [27,28]. The selection of the most appropriate product depends, of course, on topographic and extent requirements.

Generally, terrestrial photography supports observations with the following characteristics: higher spatial resolution (below 5 m), higher temporal resolution (less than 1 day), higher observation occurrence (the cloud cover has a reduced impact), and limited spatial coverage (up to 5 km²) [29]. Satellite data, like Landsat 8/9 or Sentinel2, support observations with medium spatial resolution (10–30 m), lower temporal resolutions (more than 5 days), lower observation occurrence (e.g., in Svalbard, 30% of the images are cloud-free [30]), and large spatial coverage (up to 300 km² per scene) [24]. Finally, the MODIS instrument provides observations with coarser spatial resolution (250–500 m), higher temporal resolutions (twice per day), lower observation occurrence, and larger spatial coverage (about 10° × 10° per scene) [25]. Differently, microwave remote sensing provides a deeper analysis of the snowpack, expanding its description beyond the limit of the surface layer [31,32]. The interaction between the snowpack and microwaves depends on snow dielectric properties, supporting the description of the snow wetness [33,34] and avoiding the limitations induced by the cloud cover. Higher temporal resolution (daily), medium spatial resolution (50–10 m), and large spatial coverage (80–250 km² per scene) are the additional features of microwave remote sensing [34].

As for the snow cover description, albedo and snow-water equivalent are ECVs aimed at describing the snow's microphysical properties. While the snow-water equivalent (SWE) summarizes the snow density and height [35] in the whole snowpack, the snow broadband albedo (BA) or reflectance, especially when referring to the spectral behavior of snow (SR), is strictly related to the first surface layer. The SR is controlled by snow microphysics (size and grain shape) [36] as well as by the surface slope [37] and by the surface roughness [38]. Both measurements are currently supported by ground-based observations [39,40] and by airborne or satellite sensors [41].

In this work, we adopted a multi-scale strategy by combining satellite and ground-based remote sensing. This latter component is usually approached by including manned measurements [42,43]; however, the use of automated observations has recently been growing [44,45], including different optical and other indirect techniques. The discrimination between different surface types, associated with several degrees of snow-metamorphism stages [42], enhances the description of the snow microphysical properties [46,47]. While ground-based methodologies provide high time resolutions, the spatial footprint and its consequent representativeness are limited. From this perspective, satellite optical data provide a wider spatial description of the different surface cover types, supporting the assessment of snow dynamics during the melting season. On the other hand, optical spaceborne platforms are affected by the cloud cover and by the illumination conditions in terms of revisiting time and, consequently, temporal resolution [48].

This paper represents a preliminary attempt to associate the evolution of water runoff in a periglacial environment with the occurrence of several heat waves with different degrees of intensity observed during the 2022 snow season in Ny-Ålesund (Spitsbergen, Svalbard). The final objective was to assess the impact of RoS events on the modulation of water runoff in the studied drainage catchment, including the description of the snow-melting season in terms of temporal evolution and the spatial distribution of different surface cover types.

2. Materials and Methods

The study site (Figure 1) is a periglacial area located on a peninsula that extends for about 30 km in the NW–SE direction (Brøgger Peninsula, 79°N 12°E), close to the scientific research settlement of Ny-Ålesund (Spitsbergen, Svalbard). This human settlement includes the research facilities and the airport, with a total surface area of 220,000 m². The area is surrounded by reliefs that reach a maximum elevation of 800 m a.s.l., on which several glaciers are hosted.

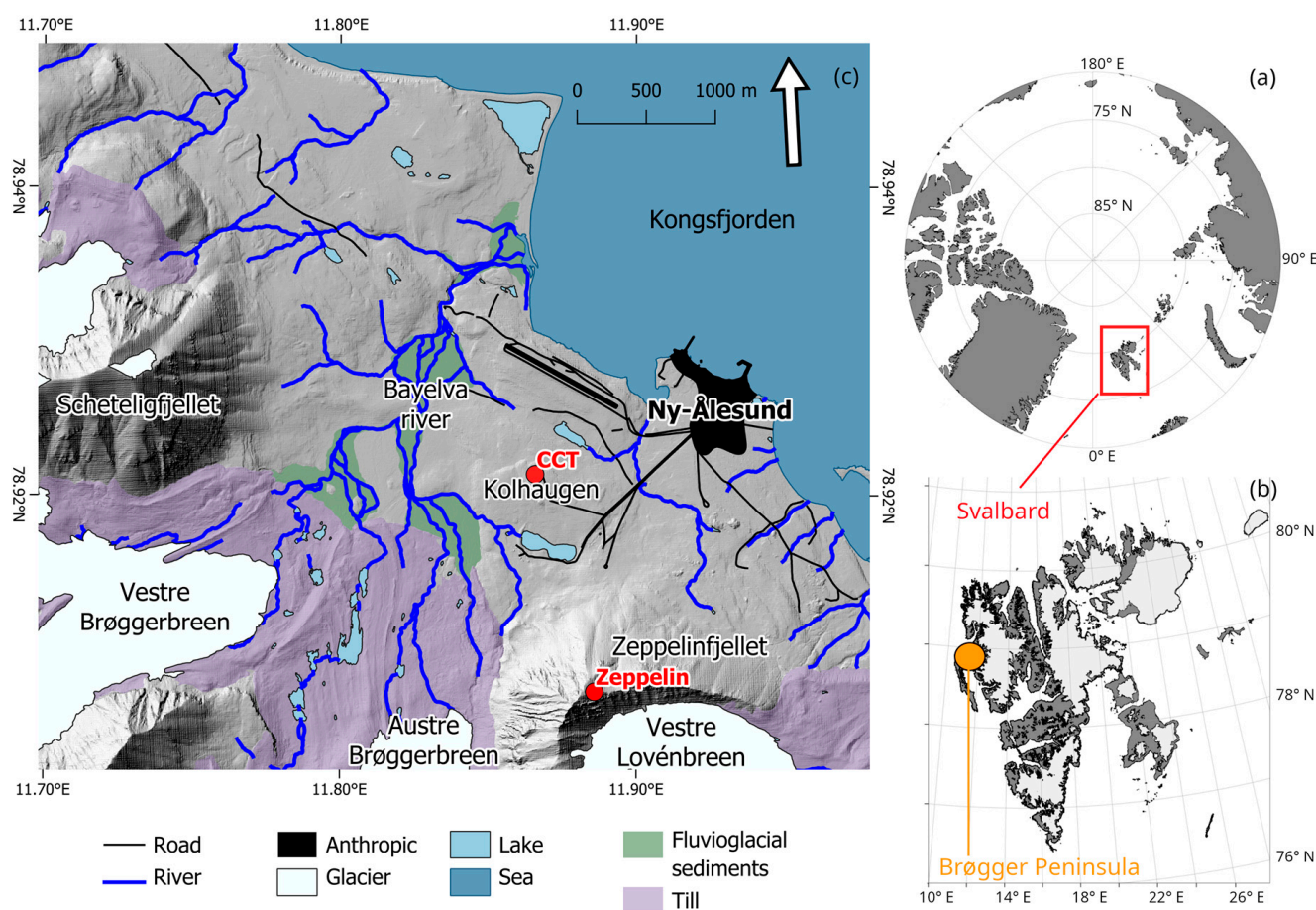


Figure 1. Location map of Svalbard (a) and of the Brogger Peninsula (b). The study area with selected geographical features (c) combined with the position of automated stations (red dot), respectively the Amundsen-Nobile Climate Change Tower (CCT) and the Zeppelin Observatory. The base map features were obtained using data from [49].

The study area is an outwash plain extending from the confluence between the Austre and the Vestre Brøggerbreen glaciers, enclosed by the Zeppelinfjellet (556 m a.s.l.) and by the Scheteligfjellet (694 m a.s.l.) on the southeast and northwest borders, respectively. The area is characterized by landforms associated with glacial and fluvio-glacial processes [49,50], where the bedrock consists of dolostones, sandstones, shales, conglomerates, and occasionally siliceous shales and limestones [50].

The considered area of interest (AOI) includes the surface covered by two time-lapse cameras located in the region (Figure 2). The AOI covers, therefore, the plain from the coastline close to Ny-Ålesund up to the glacier fronts with an extension on land of about 12 km², with a maximum altitude of 80 m above the sea level. The surface hydrology is extremely dynamic, and its most interesting feature is the occurrence of summer coastal lakes that become gradually exposed at the end of the snow-melting season from late May to late June. The study area also includes part of the Bayelva River catchment, where a water reservoir provides supply to the neighboring village.

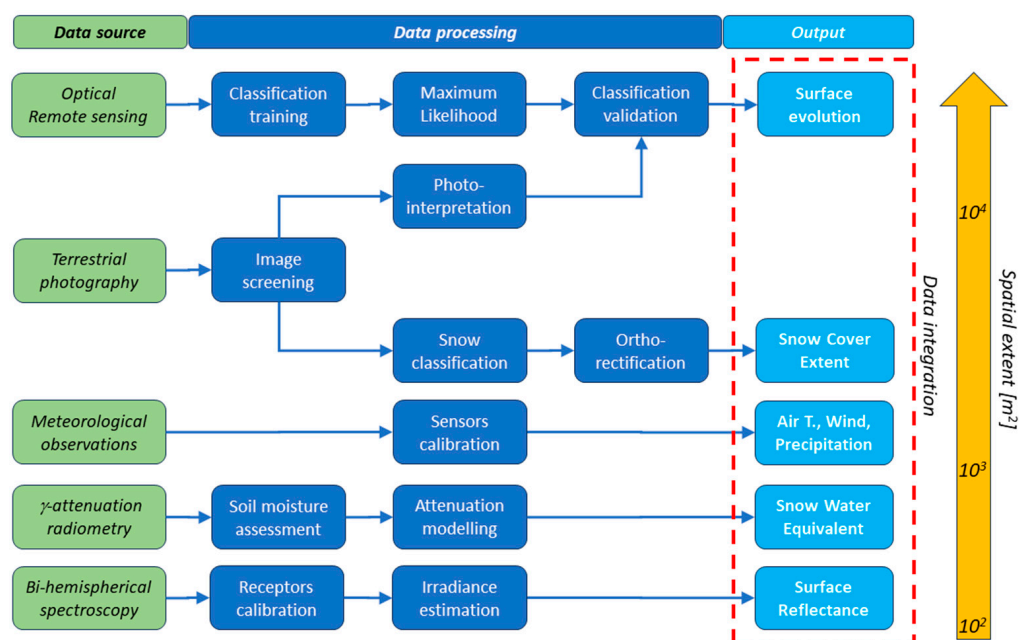


Figure 2. Flow chart of the selected data sources and the relationship between data processing steps and specific outputs.

Since 16 March 2022, the whole study area has been affected by an extreme warming event coupled with intense rainfall, which triggered an anomalous melting season between May and July 2022. The selected observation setup included ground-based and satellite platforms with different spatial and temporal resolutions, data limitations, and spatial coverage (Table 1).

Table 1. Summary of the considered observations with the description of the spatial and temporal resolutions as well as the spatial coverage.

Variable	Symbol	Unit	Spatial Resolution	Temporal Resolution ^a	Data Availability ^b	Spatial Coverage ^c
Land Cover	LC	%	10 m	~5 days	~30%	17 km ²
Air Temperature	T	°C	n.d. *	600 s	100%	1–10 km ²
Wind Speed	WS	ms ⁻¹	n.d.	120 s	100%	1–10 km ²
Precipitation	P	mm	n.d.	600 s	100%	1–10 km ²
Snow Cover Extent	SCE	%	5 m	1 day	~95%	5 km ²
Snow Water Equivalent	SWE	mm	n.d.	6 h	100%	400 m ²
Spectral Reflectance	SR		n.d.	300 s	100%	100 m ²

* n.d.: not defined; ^a highest available temporal resolution; ^b the percentage of data available in the case of specific limitations (cloud cover, sunlight, etc.); ^c the spatial extent of the observation in the area of interest.

Data integration was the strategy approached for describing the surface evolution during the snow-melting season (Figure 2).

2.1. Ground-Based Observations

Ground-based observations describing the snow cover dynamics and the meteorological conditions during the snow season were obtained by automated stations available in the study area and representative of the selected geographical framework. The meteorological station and the snow facility were located close to the Amundsen-Nobile Climate Change Tower (CCT, 78.92°N 11.86°E, 35 m a.s.l.) at the Kolhaugen site, and both have been operated by CNR since 2010.

2.1.1. Meteorological Data

Data obtained at the CCT were processed by the Italian Arctic Data Center (IADC). The available datasets provided meteorological parameters (e.g., air temperature and wind speed), detected by sensors located at 2 m above the ground. The sensor setup and data descriptions are available by looking at the specific metadata, accessible through the IADC web portal (<https://data.iadc.cnr.it/>, accessed on 29 June 2023) [51]. The daily average precipitation was estimated using data available from the Norwegian Meteorological Institute portal (<http://www.seklima.met.no/>, accessed on 29 June 2023), selecting the Ny-Ålesund station (id = SN99910). The detection of rain-on-snow episodes was assessed considering the air temperature higher than the equal-probability threshold of rain/snow precipitation (RST), defined by [37] as 0.4 °C.

2.1.2. Spectral Reflectance

The optical behavior of the snow cover on the ground was obtained by using the RoX instrument (JB Hyperspectral GmbH, Düsseldorf, Germany). The device was deployed at the snow facility and installed at 3 m above the ground in late March 2022. The instrument aims to describe the surface optical properties in the visible and near-infrared wavelength domains (400–900 nm). Two optic fibers equipped with a remote cosine receptor detected the incoming and the reflected radiative fluxes, contributing to the estimate of the bi-hemispherical reflectance [47], as in Equation (1).

$$BHR(\theta_i, \phi_i, 2\pi; 2\pi; \lambda) = \frac{d\Phi_r(\theta_i, \phi_i, 2\pi; 2\pi)}{d\Phi_i(\theta_i, \phi_i, 2\pi)}, \quad (1)$$

The bi-hemispherical spectral reflectance for each wavelength (*BHR*), produced by the sun located at different elevations (θ_i) and azimuths (ϕ_i), was estimated considering the diffuse reflected radiation (Φ_r) and the sum of the direct and the diffuse incoming radiations (Φ_i). Data were quality-checked, including an inter-calibration session at the beginning and at the end of the melting season. Measurements were obtained every 2 min and averaged every day over a 30 min temporal window, which was selected for the maximum solar elevation at 10 UTC time.

2.1.3. Snow-Cover Extent

The snow-cover extent (SCE) over the study area was estimated using the terrestrial photography approach based on ground-based cameras located at the Zeppelin Observatory (380 m a.s.l.) [52] and at the Amundsen-Nobile Climate Change Tower at 15 m above the ground [53] (Figure 3). The Zeppelin system was an Axis Q6128-E device equipped with an 8-megapixel sensor, shooting four different views of the coastal area once per day, at about 12 AM local time. The CCT system was a Sony IMX219 sensor with an 8-megapixel resolution, facing westward to the Vestre Brøggerbreen glacier front. The CCT imagery was, in this case, acquired hourly.

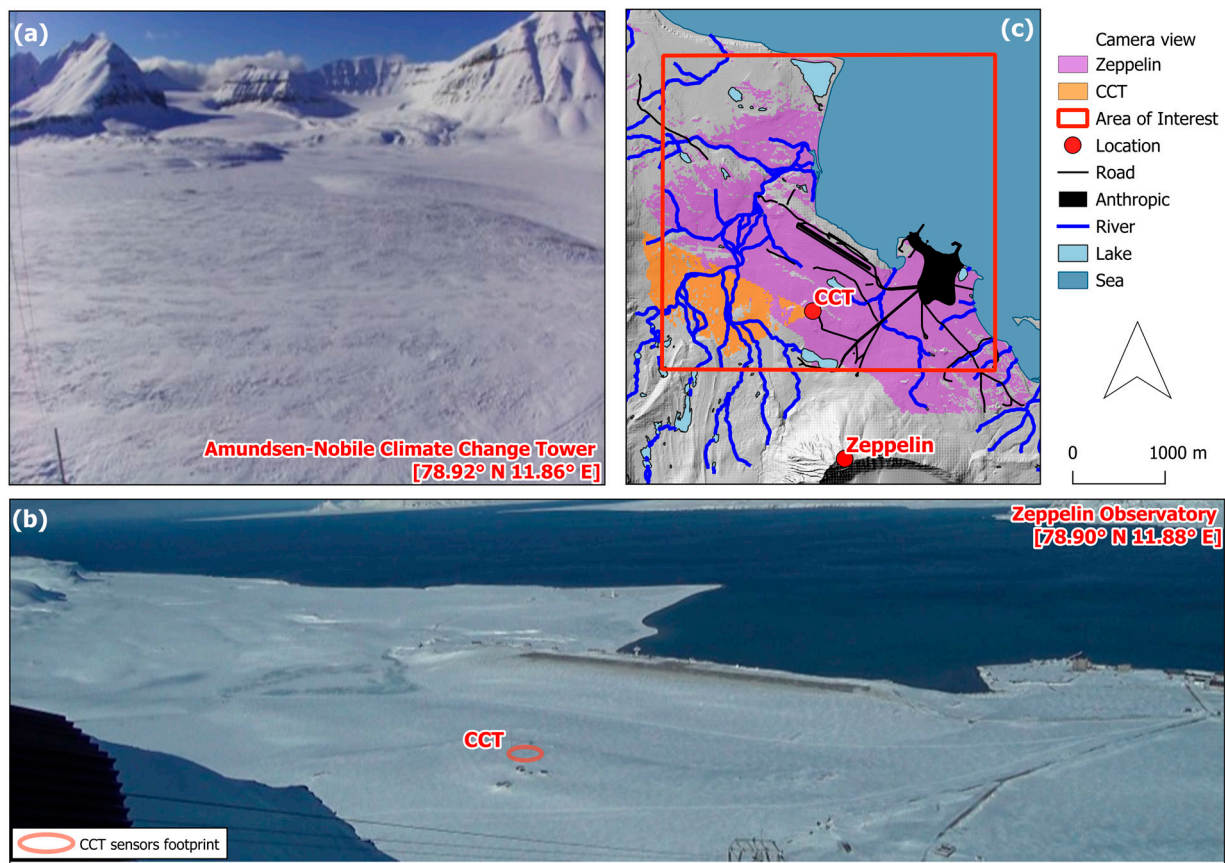


Figure 3. Camera views of the time-lapse sensors operating at the Amundsen-Nobile Climate Change Tower [49] (a) and at the Zeppelin Observatory [48] (b). Projected views obtained by the two systems in relation to the satellite AOI (c).

The available imagery was processed using the spectral similarity approach described by [54], where pixel color components (P_R, P_G, P_B) were projected into a new vector color space described by a spectral angle (θ) and a spectral distance (Δ) from a white reference vector ($R_R = 1, R_G = 1, R_B = 1$) (Equations (2a) and (2b)).

$$\theta = \cos^{-1} \frac{P_R R_R + P_G R_G + P_B R_B}{\sqrt{P_R^2 + P_G^2 + P_B^2 + \sqrt{R_R^2 + R_G^2 + R_B^2}}}, \quad (2a)$$

$$\Delta = \sqrt{P_R^2 + P_G^2 + P_B^2}, \quad (2b)$$

This vector space supported the image segmentation using the Mahalanobis distance between each pixel and the identified clusters. Finally, the identification of snow surfaces was supported by higher θ angles and lower Δ values. Snow centroids were identified considering spectral thresholds with angles higher than 0.9 and distances lower than 0.1.

The orthorectification task was supported using ten ground control points (GCPs) as well as the retrieved camera parameters obtained by a chessboard calibration. The Root Mean Square Error (RMSE) obtained by the orthorectification process was, on average, about 3.5 m, using the digital elevation model with a 5 m resolution provided by the Norwegian Polar Institute as a reference. The projected pixels were aggregated using the Sentinel-2 grid with 10 m spatial resolution and the final output of the classification algorithm was the Fractional Snow-Covered Area (FSCA) per area unit. The SCE estimation for the satellite AOI (Figure 3c) was assessed by selecting an FSCA threshold of 50% for each Sentinel-2-derived pixel. The SCE estimation comparable to the sensors deployed at the CCT was assessed considering a 400 m² plot in front of the facility (Figure 3b).

2.1.4. Snow-Water Equivalent

The snow-water equivalent (SWE) was estimated using the gamma-ray attenuation method [55] associated with the CS725 detector (Campbell Scientific, Inc., Logan, UT, USA). The instrument was installed close to the CNR snow facility at 3 m above the ground, measuring the total counts emitted by the surface (N). The gamma-ray counts associated with ^{40}K and ^{208}Tl soil emission (N_0) were estimated during the previous dry season and manned measurements at the study site were considered for validating the obtained measurements. Observations were averaged over a 6-h time range using Equation (3), described by [55].

$$SWE = \frac{1}{\beta} \ln \left(N \frac{1 + 1.11SSM}{N_0} \right), \quad (3)$$

The required parameters were also the soil moisture content during the summer period and the saturated soil moisture content (SSM). The β coefficient was a snowpack parameter produced by Campbell using their proprietary models.

2.2. Satellite Data

The detection of the surface hydrology over the study area, in the period from March to July 2022, was approached considering Sentinel-2 data. Data were obtained through the Copernicus Open Access Hub catalog, downloading L1 products and selecting ten cloud-free scenes from March to July 2022. Bands with a 20 m spatial resolution were resampled to a 10 m resolution without changing the original pixel value. The change detection analysis on the snow cover between March and June was performed using the maximum likelihood classification method. The algorithm supported the estimation of the probability of each pixel belonging to one of the identified land cover classes [56,57] (Equation (4)).

$$g_i(x) = \ln p(\omega_i) - \frac{1}{2} \ln K_i - \frac{1}{2} (x - m_i)^T K_i^{-1} (x - m_i), \quad (4)$$

This probability (g) was calculated considering the equal probability for each pixel to be classified into different classes (p). The spectral behavior of each pixel represented a vector (x) that was compared to similar mean vectors (m) defined for each selected training region of interest (ROI). Each class was characterized by a covariance matrix (K) determined for the pixel associated with each ROI.

A supervised land cover classification of the satellite images was performed, training the algorithm with ROIs identified by the visual interpretation of the RGB composite for each satellite image. Each ROI included about 200 pixels per scene, representative of snow, snow-free, freshwater, and sediment land cover classes. Snow-free areas included, in detail, bare soil and vegetation zones, as well as a mixture of both components. While the freshwater class represented lakes and streams on land, sediments indicated the detection of water-saturated covers that were generally identified in the braided river system. Since some images were affected by shadow effects, an additional class was identified for aggregating snow under shadow conditions to the snow cover class. Finally, classification statistics were assessed for each scene using a validation dataset obtained by photointerpretation performed on terrestrial imagery. The considered metrics for assessing the performance of the classification task were the overall accuracy (OA) and the kappa coefficient (κ). The first metric was defined as in Equation (5):

$$OA = \frac{\sum_{i=1}^n m_{i,i}}{N}, \quad (5)$$

considering the number of pixels used for the validation task (N), the number of classes (n), and the number of coherent pixels for each class (i) between the satellite and terrestrial datasets ($m_{i,i}$). The second metric was defined as in Equation (6), considering the total

number of pixels for each class in the satellite dataset (S_i) and the total number of pixels for each class in the terrestrial dataset (T_i):

$$\kappa = \frac{N \sum_{i=1}^n m_{i,i} - \sum_{i=1}^n S_i T_i}{N^2 - \sum_{i=1}^n S_i T_i}, \quad (6)$$

The derived confusion matrices (Tables S1–S9) supported the estimation of an average overall accuracy of about 98%.

2.3. Softwares

The data analysis was performed using scripts developed in the R programming environment 4.2.2 (<https://cran.r-project.org/>, accessed on 29 June 2023), satellite data were classified using procedures available in the ENVI software 5.7 (<https://www.nv5geospatialsoftware.com/Products/ENVI>, accessed on 29 June 2023), and, finally, spatial data were processed using the QGIS software 3.32 (<https://qgis.org/it/site/>, accessed on 29 June 2023).

3. Results

In terms of surface runoff, the evolution of the seasonal snow in Ny-Ålesund from March to July 2022 was anomalous. Ground observations supported the description of the meteo-climatic conditions and the relationships with snow dynamics and its spatial distribution. While the first part of this section is focused on presenting ground-based observations at a key site, the second part is aimed at integrating the ground truth and the satellite data.

3.1. The Meteorological Framework of the Snow Season

The evolution of the snow cover and its melting gave rise to the development of surface hydrology, both in terms of water runoff and periglacial or coastal lakes, from the glacier fronts to the coastal areas. A complete description of the surface properties in this study was approached at the Kolhaugen site where different assets are available. Spring 2022 represented a major anomaly in terms of heat wave events at the study site and, more in general, in the Svalbard area [58,59]. Several heat waves were observed (Table 2), considering a heat wave as an event with daily average temperatures significantly above the 90th percentile [5] of the decadal averages [60], which persist for at least 6 days. The event observed on 16 March as well as the one which occurred in late May were 5 °C above the 90th percentile of the decadal average. They were also associated with rain-on-snow episodes since the air temperature was higher than the equal-probability threshold of rain/snow precipitation [60].

Table 2. Summary of observed heat waves in 2022, with relevant meteorological features and associated RoS.

HW	Duration (Days)	Peak Day	T _{max} (°C)	Threshold ¹ (°C)	RoS	P (mm)
#1	6	3/7	−1.92	−3.30		
#2	7	3/15	3.13	−3.03	3/16	42.6
#3	20	6/1	7.21	0.95	5/21	22.3
#4	7	7/16	12.13	8.13		

¹ Threshold estimated as the daily average of the 90th percentile over 6 days in the reference record, 1993–2011 [5].

The March RoS was, therefore, characterized by cumulative liquid precipitation during the event above 70 mm with above-zero air temperature lasting for 96 h (Figure 4).

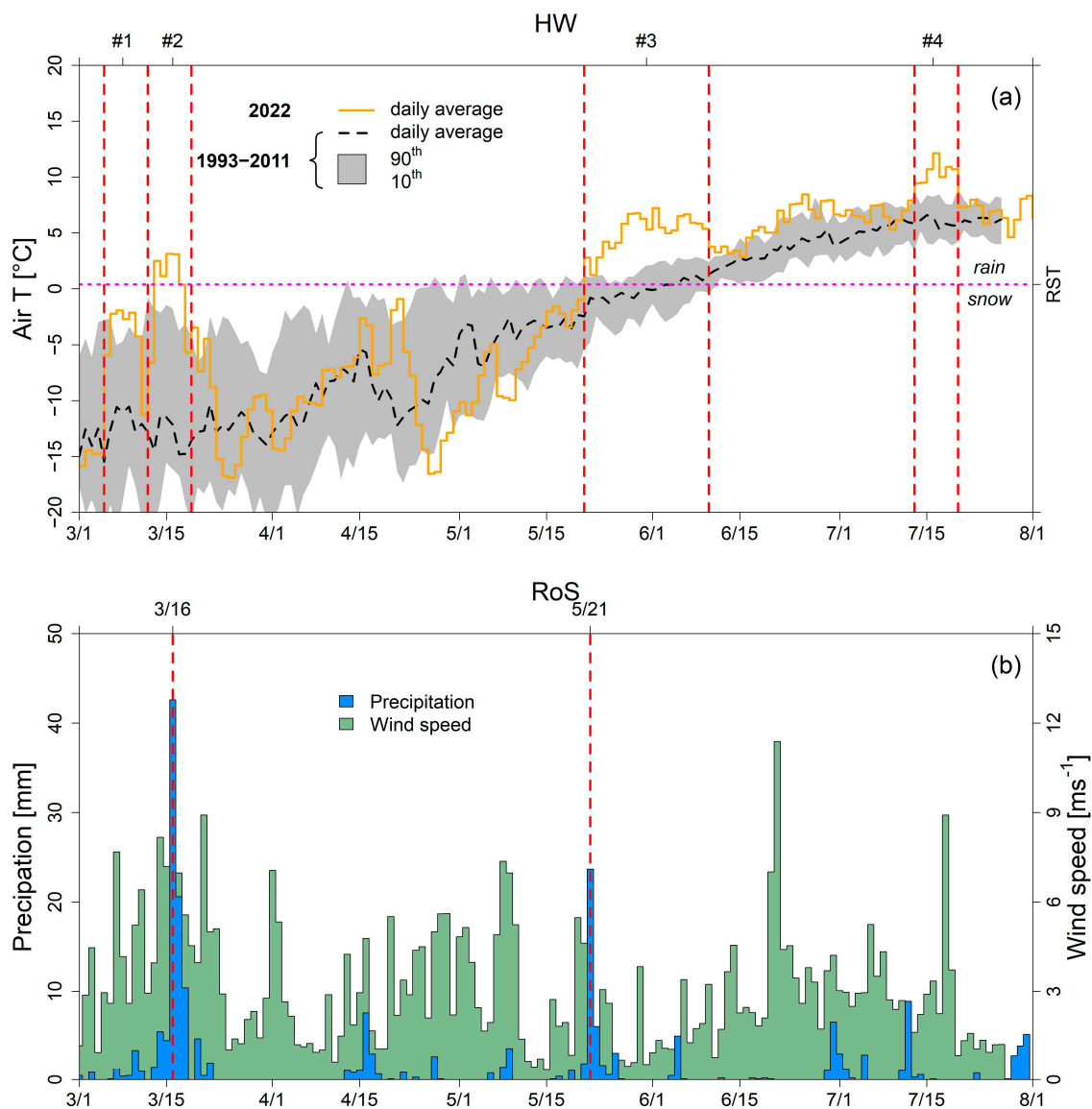


Figure 4. The meteorological framework of heat wave events occurred at Ny-Ålesund during the snow season of 2022. Heat waves were identified (as in Table 1) considering the daily air temperature average calculated for 2022 from [27] and the 90th percentile [5] of the decadal daily average calculated for the 1993–2011 period from [36] (a). Rain-on-snow events were identified (as in Table 1) considering the rain-snow equal-probability threshold (RST) [37]. Precipitations and wind speed data from [27] for the selected snow season (b).

From 21 March to 20 May, the air temperature remained below zero, reaching a minimum of below $-15\text{ }^{\circ}\text{C}$ only in April on two days. From 10 April to 20 April, a near-zero condition occurred with a snow event observed on 18 April, with 10 mm precipitation. The end of the cold period was set on 20 May, in correspondence with the May RoS, when the air temperature reached stable above-zero values continuously up to July. The triggering of the warmer season was associated with a rain event, which carried more than 20 mm of precipitation on 22 May. The period from 22 May and 1 August was characterized by air temperatures ranging between 4 and 8 $^{\circ}\text{C}$ with a maximum of 14 $^{\circ}\text{C}$. Some additional rain events with up to 10 mm of water precipitation occurred at the end of June and during July. From 20 May, a progressive phase started, with a warming associated with an increasing reduction in the snow cover (Figure 5a). The real melting season started on 20 May, after the snow accumulation phase, reducing the SCE from 100% to 0% on 19 June. The evolution of

the snow cover is summarized by the SWE dynamic, which was increasing up until 25 May (Figure 5b).

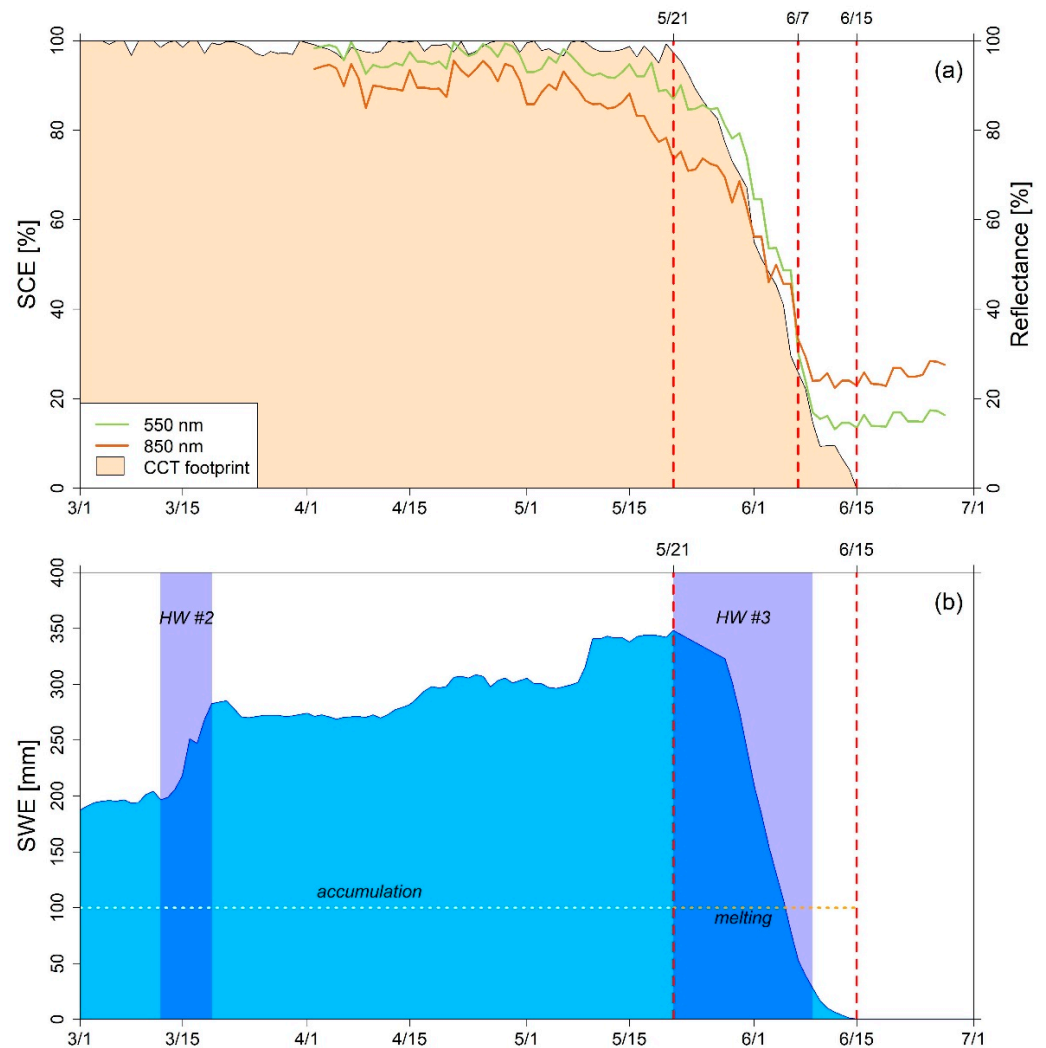


Figure 5. The evolution of the snow-cover extent (SCE) observed at the Kolhaugen site close to the CCT tower. The optical properties of the surface in the visible and near-infrared wavelength ranges (a). The evolution of the snow-water equivalent (SWE) in the snowpack during the 2022 snow season (b).

The SWE dynamic was characterized by a starting value of 200 mm in early March with three-step increments occurring on 16 March, 15–20 April, and 10 May. While two events were associated with liquid precipitation (16 March and 20 May), the slight increment that occurred on 15–20 April was related to the specific snow event. This phase was coupled also with a progressive smooth reduction in the SWE values associated with wind transport. There was another significant SWE reduction related to wind transport at the end of the second HW (in late March), but no apparent water output was detected in concomitance with the related RoS. The beginning of the warmer period by the end of May triggered the reduction in the snowpack, which decreased from 350 mm to 0 mm from 20 May to 15 June.

Looking at the evolution of the optical behavior of the snow cover, further elements were able to be detected (Figure 4a). The visible component at 550 nm was, in fact, always higher in reflectance intensity than the near-infrared wavelength values until 7 June. This behavior was stable until 21 May, with fluctuations associated with the snow evolution switching between snow deposition, snow wind transport, and snow metamorphism. The broadband albedo, in this case, varied between 0.9 and 0.8, and it decreased to less than

0.3 at the end of the snow-melting season. The snow optical behavior between late May and the end of the melting season was strongly affected by the occurrence of surface water, which is significantly radiation-absorbent in both the visible and near-infrared domains. The transition was smoother until the snow layer was thin enough to be passed by solar light and interaction with the soil layer was possible. The threshold intercepted on 7 June represented an approximate ratio between snow and soil of 40% in terms of SCE.

3.2. The Spatial Distribution of Surface Land-Cover Types Using Satellite Observations

The spatial distribution of different surface cover types during the melting season was obtained by using ten Sentinel-2 scenes (Figure 6). In addition to the expected snow disappearance, the major observations during the snow-melting season highlighted that surface fluvioglacial deposits could be detected from June as water-saturated sediments. Those deposits outcropped aligned to the drainage network that was previously developed as water output during the March event. The freshwater system was observed at different moments of the melting season and all the identified components were developed as expected during the considered period.

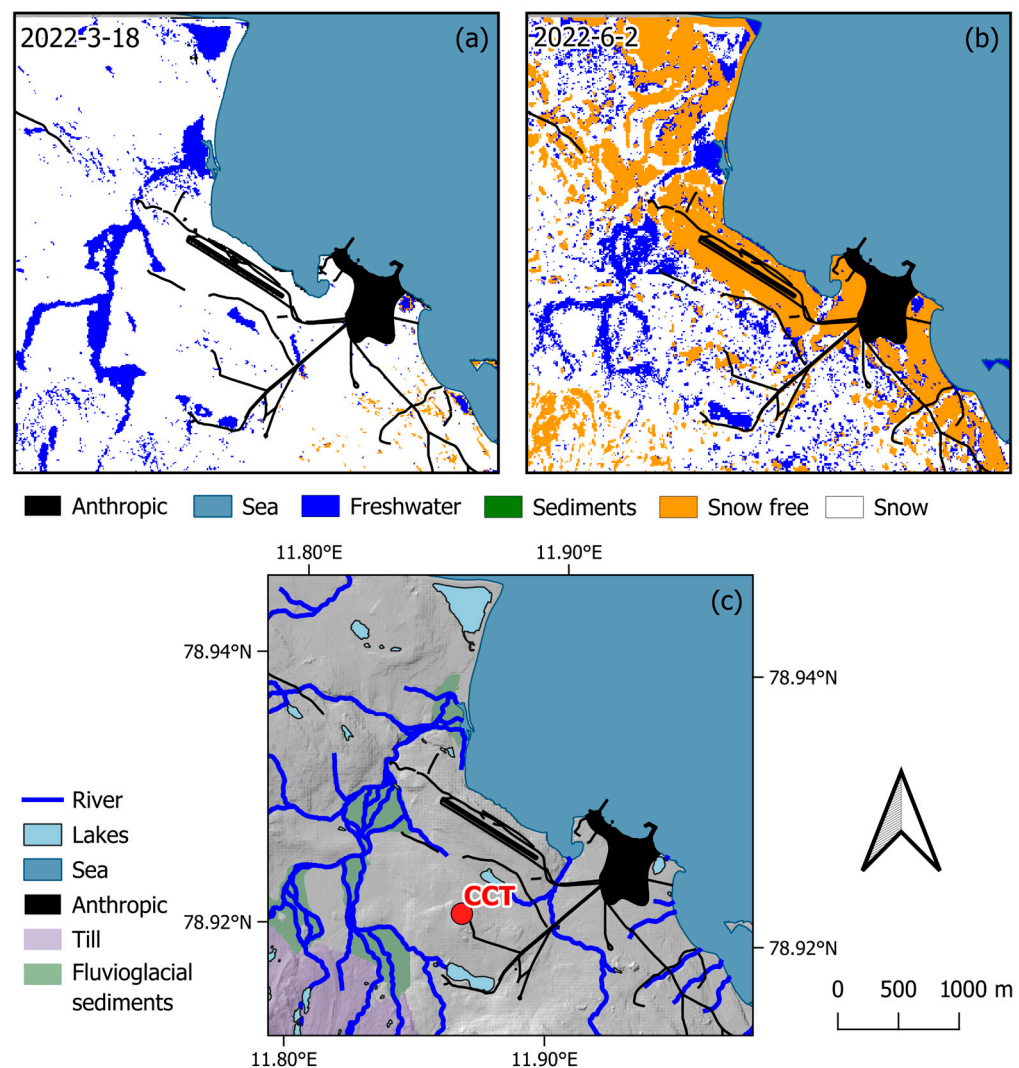


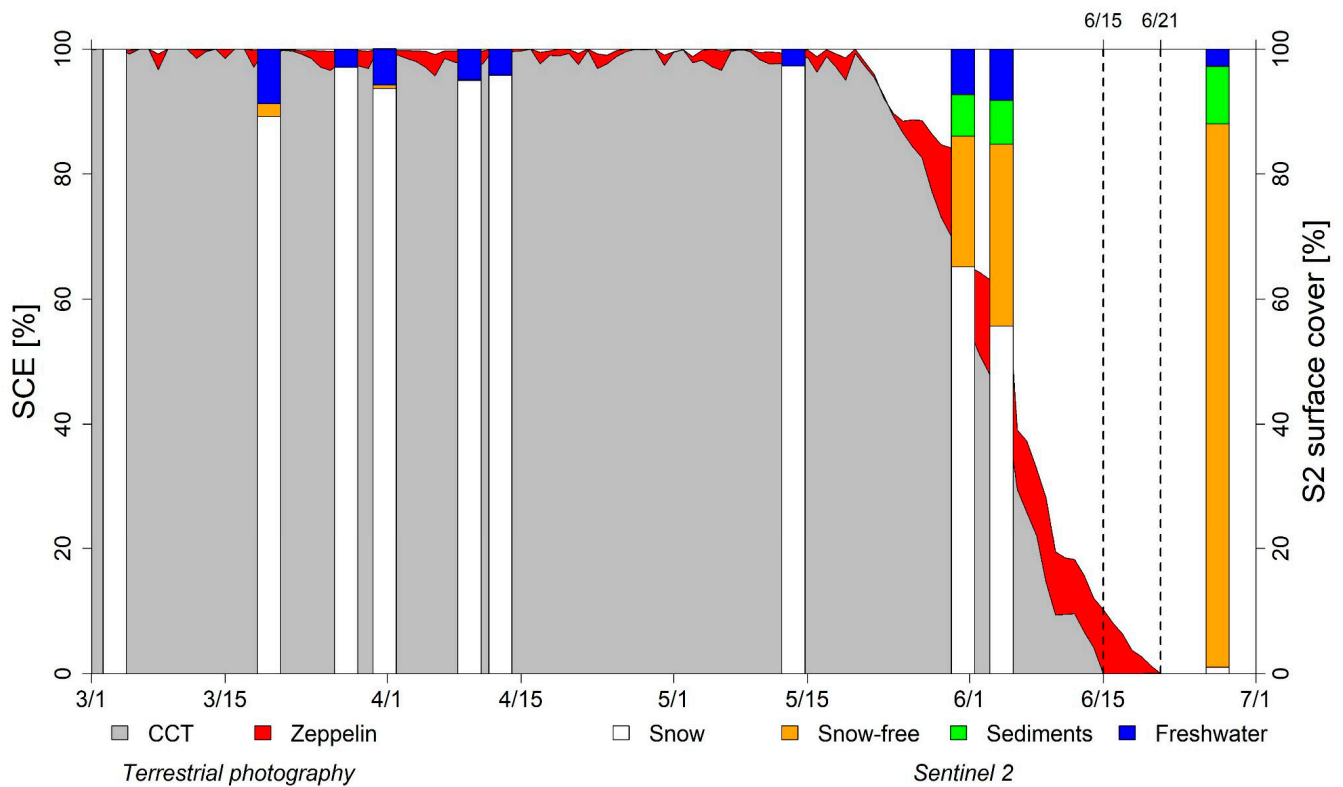
Figure 6. The evolution of the area covered by water and snow detected using Sentinel-2 data during the melting season (a,b). Geomorphological scheme of the area of interest (c).

The overall accuracy and Kappa coefficient estimated for each image highlighted the good performance of the utilized classification algorithm (Table 3).

Table 3. Classification statistics for the 10 Sentinel-2 images selected during the 2022 melting season.

Date	Overall Accuracy [%]	Kappa Coefficient
3/1	100.00	1.00
3/18	99.95	1.00
3/26	99.24	0.99
3/30	98.29	0.97
4/8	98.65	0.98
4/11	99.79	1.00
5/11	100.00	1.00
5/29	94.23	0.92
6/2	94.76	0.98
6/25	95.99	0.94

While the snow-covered areas showed a stable, high number of pixels (above 85%) until mid-May, the snow-free areas conversely evidenced a gradually increasing number of pixels as of late May (Figure 7).

**Figure 7.** Snow-cover extent and land-cover evolution of the area detected using terrestrial photography and Sentinel-2 data during the melting season.

Only the freshwater showed an extremely fluctuating pattern, which was halved in April. This can be associated with two key events occurring during the melting season: the rain-on-snow event in mid-March and the end of the melting season. These showed a freshwater surface area of about 8–9%, which was partially refrozen in late March and then discharged into the sea starting in late May (Table 4).

Table 4. The land-cover type composition in the region of interest obtained by the classification ¹ of Sentinel-2 imagery during the 2022 snow-melting season.

Date	Freshwater	Snow	Snow-Free	Sediments
3/1	0.00	100.00	0.00	0.00
3/18	8.75	89.18	2.07	0.00
3/26	2.92	97.08	0.00	0.00
3/30	5.78	93.68	0.54	0.00
4/8	4.95	94.99	0.07	0.00
4/11	4.20	95.80	0.00	0.00
5/11	2.73	97.27	0.00	0.00
5/29	7.28	65.16	20.88	6.68
6/2	8.21	55.70	29.09	7.00
6/25	2.76	1.06	86.97	9.20

¹ Seawater and anthropic areas were not included in the considered total area.

The hydrologic component of the water output (freshwater and water-saturated sediments) was 14–15% of the surface in late May–early June, which was then reduced to about 12% in late June. Although the snow-cover extent estimated using satellite data was consistent with the SCE calculated using the available time-lapse camera views, a shift was observed when limiting the analysis obtained by terrestrial photography to the footprint of sensors installed at the CCT. Considering the CCT sensors' footprint with an extent limited to 20 m distance from the observation platform, the SCE timing of the completed snow melting period was coherent on 15 June. Results obtained by satellite and terrestrial platforms, in this case looking at the whole catchment from the Zeppelin observatory, depicted the snow-off 6 days later, on 21 June (Figure 7).

4. Discussion

The snow season of 2022 in the Ny-Ålesund area showed an interesting feature associated with the combined HW–RoS event that occurred on 16 March. The developed meteorological framework caused the first significant reduction in the snow cover and the release of an important water output in late March (Figure 7). No significant SWE reduction was observed during this first warming event, highlighting that only moistening and ripening occurred in the snowpack, at least in flat areas. The capacity to store water was exceeded only close to river slopes, producing a limited volume output with a reduced capacity to percolate through the snowpack, probably due to the presence of refrozen ice layers. This picture is coherent with the one observed by [34] during a similar event in February 2017 using microwave remote sensing. The 2022 season showed a marked temperature decrease in the following days coupled with significant wind blow, refrozen surface waters, and ice crust over the snow cover. Further solid precipitation occurred until mid-May, when an additional HW–RoS combination impacted the area, triggering the start of the melting season. The Julian date of 136 for the melting onset was consistent with the earliest limit of the average melting onset (130–150) estimated for the 2004–2020 range by [34]. The SWE content fully reduced until the end of the melting season, showing a diffuse output condition in the snowpack over the whole area. The optical behavior of surface snow, even if observations started only in April, showed a stable high albedo value until early May. Secondary fluctuations of spectral components before early May were consistent with observations present in the literature [43] when fresh snow and wind transport usually occurs [45]. The visible and the near-infrared wavelength ranges showed, in fact, reflectance values above 0.8, typical of conditions where fresh snow and wind transport increase the specific surface area [43], depositing or fragmenting snow crystals with higher specific surface area (SSA) [46]. Further analyses are of course required for assessing the relationship between snow aging and optical behavior. The surface roughness and microphysical properties of surface layers (specific surface area, density, and optical equivalent radius) represent a complex issue, where snow radiative transfer modeling is a

major task that must be approached. Since May, a progressive reduction was detected both in the visible and in the near-infrared wavelength domains due to the snow melting.

The SWE and the SR evolutions were coherent with the observations obtained by terrestrial photography, which highlighted the timing of snow melting at different spatial scales. Considering the CCT footprint of sensors, with an extent limited to a 20 m distance from the observation platform where automated stations were deployed, the SWE and SCE timing of the completed snow melting period were coherent on 15 June. Results obtained by satellite and terrestrial platforms, in this case looking at the whole catchment, depicted the snow-off 6 days later, on 21 June. The Julian dates for those first days without snow, 167 and 173, respectively, fell within the average range (160–180) defined by [48] for the 2004–2019 period.

Satellite data provided deeper surface descriptors than the terrestrial photography approach: in fact, spaceborne platforms are equipped with more efficient multi-spectral sensors, which are suited for discriminating different surface types, especially for the near-infrared wavelength domain. As a matter of fact, water-saturated sediments and freshwater are strongly impacted by the presence of liquid water, which absorbs the short-wave radiative component [61]. While the March event was only characterized by freshwater collected probably on slopes located close to the drainage system, the May–June discharge was more diffused and associated with the snow melting in the whole area. The intensity of water output was so intense that it involved deeper layers in the snowpack, and water discharge involved soil and sediments. The drainage system was not only limited to free water surfaces and water bodies like rivers and lakes, but it was also extended to water-saturated sediments, as observed since late May. Unfortunately, the first drainage pulse's description was limited to the surface extent and spatial distribution, and further data are necessary to estimate the water volume that was released on the coastline. The water output released in late March 2022, after the RoS event, was spatially limited to slopes located close to the drainage system, and elevated areas such as the CCT showed a less significant decrease in SWE compared to the deposition of 70 mm of water equivalent. Debris transport to the fjord during the first HW was not identified by satellite and terrestrial imagery, preventing the detection of a brown plume close to the shoreline, as occurred in the following summer season (Figure S1). In fact, the satellite sensors' detection of debris and substances released towards the coastline started in early June, with a peak value later in the same month, highlighting an intense and large brown plume in front of the river delta. In this case, the SWE dropped from 300 mm to 0 at the CCT site. The water discharge was extended even down to the deepest layer of the snowpack, until the ground interface. The extent of water detected at the surface, from satellite observations, increased from about 8% to about 15%, considering the water-saturated sediments involved in the snow-melting season. The water volume decreased in late June, leaving only 2% of free water on the surface, but water-saturated sediments confirmed the occurrence of water discharge into the sea.

Unlike other ground-based or satellite methodologies, which already offer reliable results in identifying RoS events, the contribution of this study was focused on the description of surface evolution. As we mentioned before, surface hydrology is key information for assessing the snow melting associated with winter heatwaves, and the detection of freshwater (streams, lakes, and ponds) in concomitance with seasonal snow represents major knowledge for cryospheric studies. Surface hydrology is a task already approached in Arctic areas using both optical [61,62] and microwave remote sensing [63], but the complexity of the selected study area was in this case contributed by the simultaneous occurrence of seasonal snow, water bodies, and outcropping bedrock during the snow melting event. A key role was played by the dynamic of braided channels in the riverine system [61], and the capacity to detect water-saturated sediments was the major feature that differentiated the water output in the summer season in comparison to the winter heatwave. Despite the need for an implementation to overcome some limitations, the study

showed how the short-wave infrared sensor on board the Sentinel-2 sensors indeed can enhance the potential to discriminate different surface types in more detail.

The presented knowledge represents a key tool for assessing RoS impact in the Arctic and especially in periglacial areas. This multi-source description of the surface evolution represents an ideal background for developing a synergy between optical and microwave remote sensing. Data integration constitutes the ideal strategy for describing the snow dynamics under warm events and, nonetheless, it showed the direction of future developments. The limitations for the exact estimation of discharged water volumes constitute the grounds for future challenges, also combining water discharge's additional information with the nutrient loading.

5. Conclusions

The impact assessment of Arctic heat waves is a critical task, made even more so by considering the increase in extreme events in winter and also in association with rain-on-snow conditions. The monitoring of snow dynamics in relation to heat waves and rain events was approached in Ny-Ålesund during a peculiar snow season in 2022. The assessment was supported by a multi-scale strategy based on single-point automated stations, terrestrial photography, and satellite observations. Winter heat waves contributed to a first pulse of water output that represented a limited and localized impact of the rain-on-snow event on the snow cover. The snowpack was generally capable of retaining the rainwater, developing a winter drainage system on a surface of about 8% of the whole catchment. The second major heat wave also associated with rain-on-snow triggered the release of a larger amount of surface water that impacted the whole area. The water output even involved the deep layers of the snowpack, up to the snow-ground interface, activating the braided river system. The surface covered by water-impacted land types was doubled in extension, and the conclusive evidence involving the depth of this process was the brown plume that was developed close to the coastline.

Supplementary Materials: The following supporting information can be downloaded at: <https://www.mdpi.com/article/10.3390/rs15184435/s1>, Tables S1–S9 Statistical metrics obtained by classifications performed on Sentinel-2 scenes acquired from March to June 2022. Figure S1 Comparison between two Sentinel-2 scenes evidencing the coastal plume during the different runoff periods in 2022.

Author Contributions: Conceptualization, R.S. (Roberto Salzano) and R.S. (Rosamaria Salvatori); methodology, R.S. (Roberto Salzano) and R.S. (Rosamaria Salvatori); validation, R.S. (Roberto Salzano) and R.S. (Rosamaria Salvatori); formal analysis, R.S. (Roberto Salzano), M.S. and R.S. (Rosamaria Salvatori); investigation, R.S. (Roberto Salzano), R.C. and F.S.; data curation, R.S. (Roberto Salzano), R.S. (Rosamaria Salvatori), and M.S.; writing—original draft preparation, R.S. (Roberto Salzano) and R.S. (Rosamaria Salvatori); writing—review and editing, R.S. (Roberto Salzano), R.S. (Rosamaria Salvatori), A.T., E.V., A.S., F.S., R.C., G.E., M.S. and S.S.; visualization, R.S. (Roberto Salzano), G.E., M.S. and R.S. (Rosamaria Salvatori); supervision, R.S. (Roberto Salzano) and R.S. (Rosamaria Salvatori); funding acquisition, R.S. (Roberto Salzano), R.S. (Rosamaria Salvatori), and A.S. All authors have read and agreed to the published version of the manuscript.

Funding: This research was included in the framework of the SIOS Snow Pilot project and of the SnowCorD contribution, Research Council of Norway, project number 322387, Svalbard Integrated Arctic Earth Observing System-Knowledge Centre, operational phase 2022. It was also contributed by the iSCORE project (PRA_INFRA_2021_9), by the CRASI project (PNRA 18_00131), and by the ECOCLIMATE project (PRA 2019-0019).

Data Availability Statement: Satellite data were obtained from ESA and are available from the Copernicus Open Access Hub portal (<https://scihub.copernicus.eu>, accessed on 29 June 2023) with the permission of ESA. Meteorological data from the CCT Tower were available from the IADC web portal (<https://data.iadc.cnr.it/>, accessed on 29 June 2023) with the permissions of CNR. Precipitation data were available at the Norwegian Meteorological Institute SEKLIMA web portal (<https://www.seklima.met.no/>, accessed on 29 June 2023) with the permission of Met.no. Data referring to the snow

cover (SWE, SCE, and reflectance) can be found at <http://eprints.bice.rm.cnr.it/id/eprint/22373> (accessed on 29 June 2023).

Acknowledgments: This research was supported by the infrastructure maintained by CNR in the framework of the Dirigibile Italia Arctic Research Station. The authors acknowledge Mauro Mazzola and Angelo Viola for supporting the collected observations during the 2022 melting season. The authors thank the CNR colleagues Massimiliano Olivieri for the ICT support and Lena Rettori for English revision and spell-checking. Authors thanks the anonymous reviewers for suggestions aimed at improving the manuscript.

Conflicts of Interest: The authors declare no conflict of interest.

Abbreviations

The following abbreviations are used in this manuscript:

AOI	Area of interest
BA	Broadband albedo
BHR	Bi-hemispherical reflectance
CCT	Amundsen-Nobile Climate Change Tower
ECV	Essential Climate Variable
FSCA	Fractional Snow-Covered Area
GCOS	Global Climate Observing System
HW	Heat waves
IADC	Italian Arctic Data Center
LC	Land cover
P	Precipitation
ROI	Region of interest
RoS	Rain-on-snow
SCE	Snow-cover extent
SR	Spectral reflectance
SWE	Snow-water equivalent
T	Air temperature
WS	Wind speed

References

1. AMAP. *AMAP Arctic Climate Change Update 2021: Key Trends and Impacts*; Arctic Monitoring and Assessment Programme (AMAP): Tromsø, Norway, 2021; pp. 1–148. Available online: <https://www.amap.no/documents/download/6890/inline> (accessed on 20 June 2023).
2. Box, J.E.; Colgan, W.T.; Christensen, T.R.; Schmidt, N.M.; Lund, M.; Parmentier, F.-J.; Brown, R.; Bhatt, U.S.; Euskirchen, E.S.; Romanovsky, V.E.; et al. Key indicators of Arctic climate change: 1971–2017. *Environ. Res. Lett.* **2019**, *14*, 045010. [[CrossRef](#)]
3. Overland, J.E. Rare events in the Arctic. *Clim. Chang.* **2021**, *168*, 27. [[CrossRef](#)]
4. Perkins, S.E. A review on the scientific understanding of heatwaves—Their measurement, driving mechanisms, and changes at the global scale. *Atmos. Res.* **2015**, *164–165*, 242–267. [[CrossRef](#)]
5. Russo, S.; Sillmann, J.; Fischer, E.M. Top ten European heatwaves since 1950 and their occurrence in the coming decades. *Environ. Res. Lett.* **2015**, *10*, 124003. [[CrossRef](#)]
6. Rennert, K.J.; Roe, G.; Putkonen, J.; Bitz, C.M. Soil Thermal and Ecological Impacts of Rain on Snow Events in the Circumpolar Arctic. *J. Clim.* **2009**, *22*, 2302–2315. [[CrossRef](#)]
7. Hjort, J.; Karjalainen, O.; Aalto, J.; Westermann, S.; Romanovsky, V.E.; Nelson, F.E.; Luoto, M. Degrading permafrost puts Arctic infrastructure at risk by mid-century. *Nat. Commun.* **2018**, *9*, 5147. [[CrossRef](#)] [[PubMed](#)]
8. Ford, J.; McDowell, G.; Pearce, T. The adaptation challenge in the Arctic. *Nat. Clim. Chang.* **2015**, *5*, 1046–1053. [[CrossRef](#)]
9. Cohen, J.; Screen, J.A.; Furtado, J.C.; Barlow, M.; Whittleston, D.; Coumou, D.; Francis, J.; Dethloff, K.; Entekhabi, D.; Overland, J.; et al. Recent Arctic amplification and extreme mid-latitude weather. *Nat. Geosci.* **2014**, *7*, 627–637. [[CrossRef](#)]
10. Bjerke, J.W.; Bokhorst, S.; Callaghan, T.V.; Phoenix, G.K. Persistent reduction of segment growth and photosynthesis in a widespread and important sub-Arctic moss species after cessation of three years of experimental winter warming. *Funct. Ecol.* **2017**, *31*, 127–134. [[CrossRef](#)]
11. Peeters, B.; Pedersen, Å.Ø.; Loe, L.E.; Isaksen, K.; Veiberg, V.; Stien, A.; Kohler, J.; Gallet, J.C.; Aanes, R.; Hansen, B.B. Spatiotemporal patterns of rain-on-snow and basal ice in high Arctic Svalbard: Detection of a climate-cryosphere regime shift. *Environ. Res. Lett.* **2019**, *14*, 015002. [[CrossRef](#)]

12. Hansen, B.B.; Isaksen, K.; Benestad, R.E.; Kohler, J.; Pedersen, Å.Ø.; Loe, L.E.; Coulson, S.J.; Larsen, J.O.; Varpe, Ø. Warmer and wetter winters: Characteristics and implications of an extreme weather event in the High Arctic. *Environ. Res. Lett.* **2014**, *9*, 114021. [[CrossRef](#)]
13. Bokhorst, S.; Bjerke, J.W.; Phoenix, G.K.; Jaakola, L.; Mæhre, H.K.; Tømmervik, H. Sub-arctic mosses and lichens show idiosyncratic responses to combinations of winter heatwaves, freezing and nitrogen deposition. *Physiol. Plant.* **2023**, *175*, e13882. [[CrossRef](#)]
14. Messori, G.; Woods, C.; Caballero, R. On the Drivers of Wintertime Temperature Extremes in the High Arctic. *J. Clim.* **2018**, *31*, 1597–1618. [[CrossRef](#)]
15. Russo, S.; Dosio, A.; Graversen, R.G.; Sillmann, J.; Carrao, H.; Dunbar, M.B.; Singleton, A.; Montagna, P.; Barbola, P.; Vogt, J.V. Magnitude of extreme heat waves in present climate and their projection in a warming world. *J. Geophys. Res. Atmos.* **2014**, *119*, 12–500. [[CrossRef](#)]
16. Dobricic, S.; Russo, S.; Pozzoli, L.; Wilson, J.; Vignati, E. Increasing occurrence of heat waves in the terrestrial Arctic. *Environ. Res. Lett.* **2020**, *15*, 024022. [[CrossRef](#)]
17. Serreze, M.C.; Gustafson, J.; Barrett, A.P.; Druckenmiller, M.L.; Fox, S.; Voveris, J.; Stroeve, J.; Sheffield, B.; Forbes, B.C.; Rasmus, S. Arctic rain on snow events: Bridging observations to understand environmental and livelihood impacts. *Environ. Res. Lett.* **2021**, *16*, 105009. [[CrossRef](#)]
18. Sobota, I.; Weckwerth, P.; Grajewski, T. Rain-On-Snow (ROS) events and their relations to snowpack and ice layer changes on small glaciers in Svalbard, the high Arctic. *J. Hydrol.* **2020**, *590*, 125279. [[CrossRef](#)]
19. Box, J.E.; Wehrlé, A.; van As, D.; Fausto, R.S.; Kjeldsen, K.K.; Dachauer, A.; Ahlstrøm, A.P.; Picard, G. Greenland ice sheet rainfall, heat and albedo feedback impacts from the mid-August 2021 atmospheric river. *Geophys. Res. Lett.* **2022**, *49*, e2021GL097356. [[CrossRef](#)]
20. Westermann, S.; Boike, J.; Langer, M.; Schuler, T.V.; Eitzelmüller, B. Modeling the impact of wintertime rain events on the thermal regime of permafrost. *Cryosphere* **2011**, *5*, 945–959. [[CrossRef](#)]
21. Nakamura, T.; Sato, T. A possible linkage of Eurasian heat wave and East Asian heavy rainfall in Relation to the Rapid Arctic warming. *Environ. Res.* **2022**, *209*, 112881. [[CrossRef](#)]
22. Jennings, K.S.; Winchell, T.S.; Livneh, B.; Molotch, N.P. Spatial variation of the rain–snow temperature threshold across the Northern Hemisphere. *Nat. Commun.* **2018**, *9*, 1148. [[CrossRef](#)] [[PubMed](#)]
23. GCOS. *GCOS 2022 Implementation Plan*; WMO: Geneva, Switzerland, 2022; Available online: https://library.wmo.int/doc_num.php?explnum_id=11317 (accessed on 20 June 2023).
24. Gascoïn, S.; Barrou Dumont, Z.; Deschamps-Berger, C.; Marti, F.; Salgues, G.; López-Moreno, J.I.; Revuelto, J.; Michon, T.; Schattan, P.; Hagolle, O. Estimating Fractional Snow Cover in Open Terrain from Sentinel-2 Using the Normalized Difference Snow Index. *Remote Sens.* **2020**, *12*, 2904. [[CrossRef](#)]
25. Stillinger, T.; Rittger, K.; Raleigh, M.S.; Michell, A.; Davis, R.E.; Bair, E.H. Landsat, MODIS, and VIIRS snow cover mapping algorithm performance as validated by airborne lidar datasets. *Cryosphere* **2023**, *17*, 567–590. [[CrossRef](#)]
26. Richiardi, C.; Blonda, P.; Rana, F.M.; Santoro, M.; Tarantino, C.; Vicario, S.; Adamo, M. A Revised Snow Cover Algorithm to Improve Discrimination between Snow and Clouds: A Case Study in Gran Paradiso National Park. *Remote Sens.* **2021**, *13*, 1957. [[CrossRef](#)]
27. Toth, C.; Jóźków, G. Remote sensing platforms and sensors: A survey. *ISPRS J. Photogramm. Remote Sens.* **2016**, *115*, 22–36. [[CrossRef](#)]
28. Valenzuela, A.; Reinke, K.; Jones, S. A new metric for the assessment of spatial resolution in satellite imagers. *Int. J. Appl. Earth Obs.* **2022**, *114*, 103051. [[CrossRef](#)]
29. Parajka, J.; Haas, P.; Kirnbauer, R.; Jansa, J.; Blöschl, G. Potential of time-lapse photography of snow for hydrological purposes at the small catchment scale. *Hydrol. Process.* **2012**, *26*, 3327–3337. [[CrossRef](#)]
30. Karlsen, S.R.; Stendardi, L.; Tømmervik, H.; Nilsen, L.; Arntzen, I.; Cooper, E.J. Time-Series of Cloud-Free Sentinel-2 NDVI Data Used in Mapping the Onset of Growth of Central Spitsbergen, Svalbard. *Remote Sens.* **2021**, *13*, 3031. [[CrossRef](#)]
31. Hallikainen, M.; Lemmetyinen, J.; Jiang, L. Snow Properties from Passive Microwave. In *Comprehensive Remote Sensing*; Liang, S., Ed.; Elsevier: Amsterdam, The Netherlands, 2018; Volume 4, pp. 224–236. [[CrossRef](#)]
32. Frei, A.; Tedesco, M.; Lee, S.; Foster, J.; Hall, D.K.; Kelly, R.; Robinson, D.A. A review of global satellite-derived snow products. *Adv. Space Res.* **2012**, *50*, 1007–1029. [[CrossRef](#)]
33. Nagler, T.; Rott, H.; Ripper, E.; Bippus, G.; Hetzenecker, M. Advancements for Snowmelt Monitoring by Means of Sentinel-1 SAR. *Remote Sens.* **2016**, *8*, 348. [[CrossRef](#)]
34. Vickers, H.; Malnes, E.; Eckerstorfer, M. A Synthetic Aperture Radar Based Method for Long Term Monitoring of Seasonal Snowmelt and Wintertime Rain-On-Snow Events in Svalbard. *Front. Earth Sci.* **2022**, *10*, 868945. [[CrossRef](#)]
35. Egli, L.; Jonas, T.; Meister, R. Comparison of different automatic methods for estimating snow water equivalent. *Cold Reg. Sci. Technol.* **2009**, *57*, 107–115. [[CrossRef](#)]
36. Domine, F.; Salvatori, R.; Legagneux, L.; Salzano, R.; Fily, M.; Casacchia, R. Correlation between the specific surface area and the shortwave infrared (SWIR) reflectance of snow. *Cold Reg. Sci. Technol.* **2006**, *46*, 60–68. [[CrossRef](#)]
37. Picard, G.; Dumont, M.; Lamare, M.; Tuzet, F.; Larue, F.; Pirazzini, R.; Arnaud, L. Spectral albedo measurements over snow-covered slopes: Theory and slope effect corrections. *Cryosphere* **2020**, *14*, 1497–1517. [[CrossRef](#)]

38. Manninen, T.; Anttila, K.; Jääskeläinen, E.; Riihelä, A.; Peltoniemi, J.; Räisänen, P.; Lahtinen, P.; Siljamo, N.; Thölix, L.; Meinander, O.; et al. Effect of small-scale snow surface roughness on snow albedo and reflectance. *Cryosphere* **2021**, *15*, 793–820. [[CrossRef](#)]
39. Kinar, N.J.; Pomeroy, J.W. Measurement of the physical properties of the snowpack. *Rev. Geophys.* **2015**, *53*, 481–544. [[CrossRef](#)]
40. Pirazzini, R.; Leppänen, L.; Picard, G.; Lopez-Moreno, J.I.; Marty, C.; Macelloni, G.; Kontu, A.; Von Lerber, A.; Tanis, C.M.; Schneebeli, M.; et al. European In-Situ Snow Measurements: Practices and Purposes. *Sensors* **2018**, *18*, 2016. [[CrossRef](#)] [[PubMed](#)]
41. Gabarró, C.; Hughes, N.; Wilkinson, J.; Bertino, L.; Bracher, A.; Diehl, T.; Dierking, W.; Gonzalez-Gambau, V.; Lavergne, T.; Madurell, T.; et al. Improving satellite-based monitoring of the polar regions: Identification of research and capacity gaps. *Front. Remote Sens.* **2023**, *4*, 952091. [[CrossRef](#)]
42. Fierz, C.; Armstrong, R.L.; Durand, Y.; Etchevers, P.; Greene, E.; McClung, D.M.; Nishimura, K.; Satyawali, P.K.; Sokratov, S.A. The International Classification for Seasonal Snow on the Ground. In *IHP-VII Technical Documents in Hydrology N°83, IACS Contribution N°1*; UNESCO-IHP: Paris, France, 2009; pp. 1–81.
43. Salvatori, R.; Salzano, R.; Valt, M.; Cerrato, R.; Ghergo, S. The Collection of Hyperspectral Measurements on Snow and Ice Covers in Polar Regions (SISpec 2.0). *Remote Sens.* **2022**, *14*, 2213. [[CrossRef](#)]
44. Scoto, F.; Pappacogli, G.; Mazzola, M.; Donato, A.; Salzano, R.; Monzali, M.; de Blasi, F.; Larose, C.; Gallet, J.C.; Decesari, S.; et al. Automated observation of physical snowpack properties in Ny-Ålesund. *Front. Earth Sci.* **2023**, *11*, 1123981. [[CrossRef](#)]
45. Salzano, R.; Lanconelli, C.; Esposito, G.; Giusto, M.; Montagnoli, M.; Salvatori, R. On the Seasonality of the Snow Optical Behaviour at Ny Ålesund (Svalbard Islands, Norway). *Geosciences* **2021**, *11*, 112. [[CrossRef](#)]
46. Kokhanovsky, A.; Lamare, M.; Di Mauro, B.; Picard, G.; Arnaud, L.; Dumont, M.; Tuzet, F.; Brockmann, C.; Box, J.E. On the reflectance spectroscopy of snow. *Cryosphere* **2018**, *12*, 2371–2382. [[CrossRef](#)]
47. Kokhanovsky, A.; Di Mauro, B.; Garzonio, R.; Colombo, R. Retrieval of dust properties from spectral snow reflectance measurements. *Front. Environ. Sci.* **2021**, *9*, 644551. [[CrossRef](#)]
48. Vickers, H.; Karlsen, S.R.; Malnes, E. A 20-Year MODIS-Based Snow Cover Dataset for Svalbard and Its Link to Phenological Timing and Sea Ice Variability. *Remote Sens.* **2020**, *12*, 1123. [[CrossRef](#)]
49. Norwegian Polar Institute. *Kartdata Svalbard 1:100 000 (S100 Kartdata)/Map Data [Data Set]*; Norwegian Polar Institute: Tromsø, Norway, 2014. [[CrossRef](#)]
50. Miccadei, E.; Piacentini, T.; Berti, C. Geomorphological features of the Kongsfjorden area: Ny-Ålesund, Blomstrandøya (NW Svalbard, Norway). *Rend. Fis. Acc. Lincei* **2016**, *27*, 217–228. [[CrossRef](#)]
51. Mazzola, M.; Viola, A.P.; Lanconelli, C.; Vitale, V. Atmospheric observations at the Amundsen-Nobile Climate Change Tower in Ny-Ålesund, Svalbard. *Rend. Fis. Acc. Lincei* **2016**, *27*, 7–18. [[CrossRef](#)]
52. Pedersen, C. *Zeppelin Web Camera Time-Series*; Norwegian Polar Institute: Tromsø, Norway, 2013. [[CrossRef](#)]
53. Salzano, R.; Aalstad, K.; Boldrini, E.; Gallet, J.C.; Kejski, D.; Luks, B.; Nilsen, L.; Salvatori, R.; Westermann, S. Terrestrial Photography Applications on Snow Cover in Svalbard (PASSES). In *SESS Report 2020—The State of Environmental Science in Svalbard—An Annual Report*; Svalbard Integrated Arctic Earth Observing System: Longyearbyen, Norway, 2021. [[CrossRef](#)]
54. Salzano, R.; Salvatori, R.; Valt, M.; Giuliani, G.; Chatenoux, B.; Ioppi, L. Automated Classification of Terrestrial Images: The Contribution to the Remote Sensing of Snow Cover. *Geosciences* **2019**, *9*, 97. [[CrossRef](#)]
55. Choquette, Y.; Lavigne, P.; Nadeau, M.; Ducharme, P.; Martin, J.P.; Houdayer, A.; Rogoza, J. GMON, A New Sensor for Snow Water Equivalent via Gamma Monitoring. In *Proceedings of the International Snow Science Workshop*, Whistler, BC, Canada, 21–27 September 2008.
56. Jensen, J.R. *Introductory Digital Image Processing: A Remote Sensing Perspective*, 4th ed.; Pearson: Glenview, IL, USA, 2015; pp. 1–590.
57. Rees, W.G. *Remote Sensing of Snow and Ice*; CRC Press—Taylor & Francis Group: Boca Raton, FL, USA, 2006; pp. 1–285.
58. Repp, K. The Hydrology of Bayelva, Spitsbergen. *Hydrol. Res.* **1988**, *19*, 259–268. [[CrossRef](#)]
59. Nowak, A.; Hodson, A. Hydrological response of a High-Arctic catchment to changing climate over the past 35 years: A case study of Bayelva watershed, Svalbard. *Polar Res.* **2013**, *32*, 19691. [[CrossRef](#)]
60. Maturilli, M.; Herber, A.; König-Langlo, G. Climatology and time series of surface meteorology in Ny-Ålesund, Svalbard. *Earth Syst. Sci. Data* **2013**, *5*, 155–163. [[CrossRef](#)]
61. Wołoszyn, A.; Owczarek, Z.; Wieczorek, I.; Kasprzak, M.; Strzelecki, M.C. Glacial Outburst Floods Responsible for Major Environmental Shift in Arctic Coastal Catchment, Rekvedbukta, Albert I Land, Svalbard. *Remote Sens.* **2022**, *14*, 6325. [[CrossRef](#)]
62. Nitze, I.; Grosse, G.; Jones, B.M.; Arp, C.D.; Ulrich, M.; Fedorov, A.; Veremeeva, A. Landsat-Based Trend Analysis of Lake Dynamics across Northern Permafrost Regions. *Remote Sens.* **2017**, *9*, 640. [[CrossRef](#)]
63. Vickers, H.; Malnes, E.; Høgda, K.-A. Long-Term Water Surface Area Monitoring and Derived Water Level Using Synthetic Aperture Radar (SAR) at Altevåtn, a Medium-Sized Arctic Lake. *Remote Sens.* **2019**, *11*, 2780. [[CrossRef](#)]

Disclaimer/Publisher’s Note: The statements, opinions and data contained in all publications are solely those of the individual author(s) and contributor(s) and not of MDPI and/or the editor(s). MDPI and/or the editor(s) disclaim responsibility for any injury to people or property resulting from any ideas, methods, instructions or products referred to in the content.